

# Accelerated and Quantitative 3D Semisolid MT/CEST Imaging using a Generative Adversarial Network (GAN-CEST)

Jonah Weigand-Whittier<sup>1</sup>, Maria Sedykh<sup>2</sup>, Kai Herz<sup>3,4</sup>, Jaume Coll-Font<sup>1,5</sup>, Anna N. Foster<sup>1,5</sup>, Elizabeth R. Gerstner<sup>6</sup>, Christopher Nguyen<sup>1,5,7</sup>, Moritz Zaiss<sup>2,3</sup>, Christian T. Farrar<sup>1\*</sup>, Or Perlman<sup>1,8,9\*</sup>✉

<sup>1</sup>Athinoula A. Martinos Center for Biomedical Imaging, Department of Radiology, Massachusetts General Hospital and Harvard Medical School, Charlestown, MA, USA

<sup>2</sup>Department of Neuroradiology, Friedrich-Alexander Universität Erlangen-Nürnberg (FAU), University Hospital Erlangen, Erlangen, Germany

<sup>3</sup>Magnetic Resonance Center, Max Planck Institute for Biological Cybernetics, Tübingen, Germany

<sup>4</sup>Department of Biomedical Magnetic Resonance, University of Tübingen, Tübingen, Germany

<sup>5</sup>Cardiovascular Research Center, Cardiology Division, Massachusetts General Hospital, Charlestown, MA, USA

<sup>6</sup>Massachusetts General Hospital Cancer Center, Harvard Medical School, Boston, MA, USA

<sup>7</sup>Health Science Technology, Harvard-MIT, Cambridge, MA, USA

<sup>8</sup>Department of Biomedical Engineering, Tel Aviv University, Tel Aviv, Israel

<sup>9</sup>Sagol School of Neuroscience, Tel Aviv University, Tel Aviv, Israel

\*C.T.F. and O.P. contributed equally to this work.

✉ **Correspondence to:** Or Perlman, Department of Biomedical Engineering, Tel Aviv University, Tel Aviv 6997801, Israel. Email: orperlman@tauex.tau.ac.il

## Content:

Words in main text: 3915

Figures: 8

Tables: 1

Supporting Information Figures: 1

**Submitted to Magnetic Resonance in Medicine**

## Abstract

**Purpose:** To substantially shorten the acquisition time required for quantitative 3D chemical exchange saturation transfer (CEST) and semisolid magnetization transfer (MT) imaging and allow for rapid chemical exchange parameter map reconstruction.

**Methods:** Three-dimensional CEST and MT magnetic resonance fingerprinting (MRF) datasets of L-arginine phantoms, whole-brains, and calf muscles from healthy volunteers, cancer patients, and cardiac patients were acquired using 3T clinical scanners at 3 different sites, using 3 different scanner models and coils. A generative adversarial network supervised framework (GAN-CEST) was then designed and trained to learn the mapping from a reduced input data space to the quantitative exchange parameter space, while preserving perceptual and quantitative content.

**Results:** The GAN-CEST 3D acquisition time was 42-52 seconds, 70% shorter than CEST-MRF. The quantitative reconstruction of the entire brain took 0.8 seconds. An excellent agreement was observed between the ground truth and GAN-based L-arginine concentration and pH values (Pearson's  $r > 0.97$ , NRMSE  $< 1.5\%$ ). GAN-CEST images from a brain-tumor subject yielded a semi-solid volume fraction and exchange rate NRMSE of  $3.8 \pm 1.3\%$  and  $4.6 \pm 1.3\%$ , respectively, and SSIM of  $96.3 \pm 1.6\%$  and  $95.0 \pm 2.4\%$ , respectively. The mapping of the calf-muscle exchange parameters in a cardiac patient, yielded NRMSE  $< 7\%$  and SSIM  $> 94\%$  for the semi-solid exchange parameters. In regions with large susceptibility artifacts, GAN-CEST has demonstrated improved performance and reduced noise compared to MRF.

**Conclusion:** GAN-CEST can substantially reduce the acquisition time for quantitative semisolid MT/CEST mapping, while retaining performance even when facing pathologies and scanner models that were not available during training.

**Keywords:** Magnetic Resonance Fingerprinting (MRF), Chemical Exchange Saturation Transfer (CEST), Magnetization Transfer (MT), pH, Quantitative Imaging, Generative Adversarial Network (GAN).

# 1. Introduction

Since the accidental discovery of magnetization transfer (MT) in 1989, semisolid MT and chemical exchange saturation transfer (CEST) have been developed as magnetic resonance imaging (MRI) contrast techniques for detecting millimolar concentrations of mobile proteins, lipids, and metabolites in-vivo.<sup>1,2</sup> Until recently, however, most CEST imaging protocols provided mostly semi-quantitative contrast by way of a full Z-spectrum acquisition followed by the magnetization transfer ratio asymmetry ( $MTR_{asym}$ ) analysis. The  $MTR_{asym}$  metric is dependent on numerous factors such as chemical exchange rate, volume fraction of the exchangeable solute protons, water longitudinal relaxation rate, radiofrequency (RF) saturation time, RF saturation power, and water transverse relaxation rate, all of which must be modeled across a variety of exchangeable proton pools.<sup>3,4</sup> Additionally, traditional CEST MRI requires long acquisition times, which limits its clinical integration.

Recently, many of these issues have been ameliorated with the development of magnetic resonance fingerprinting (MRF).<sup>5</sup> This quantitative imaging paradigm uses pseudo-random acquisition schedules to acquire unique signal trajectories, which are then matched to an existing database or “dictionary” of Bloch-equation-based simulated signals, providing a de-facto pixelwise estimation of the underlying magnetic properties. Although initially developed for water  $T_1$  and  $T_2$  relaxation time quantification, MRF has been modified and expanded for the quantification of semisolid MT and CEST parameters.<sup>4,6,7</sup> Pathological semisolid MT/CEST scenarios involve a multitude of proton pools, where several exchange parameters vary simultaneously. This leads to an exponential growth in dictionary size and hence very long dictionary generation and parameter matching times. Recently, several deep-learning-based approaches have been developed for shortening the reconstruction part of the semisolid MT/CEST MRF imaging pipeline.<sup>8,9</sup> While these strategies have demonstrated promising results, the acquisition time is still long and requires the acquisition of  $T_1$ ,  $T_2$ , and

$B_0$  maps, constituting an obstacle for routine clinical adoption.<sup>10</sup> Moreover, applying CEST-MRF for multi-slice imaging would further increase the scan time.

Recently, a unique machine learning approach has demonstrated the ability to learn the hidden and complicated relations (manifold) between two paired image categories<sup>11</sup> and generate an approximation of the appropriate image-pair for a given input. This approach, termed conditional generative adversarial network (GAN),<sup>12</sup> is built on two competing neural networks, a generator and a discriminator, which are trained simultaneously. The generator aims to synthesize convincingly realistic samples while the discriminator estimates the probability that a sample comes from the training data category.<sup>13</sup> During training, the generator gradually learns to create more convincing models based on the discriminator's feedback. The GAN framework is highly modular, and adversarial models have been shown to be effective for a variety of applications. In particular, the conditional GAN "pix2pix" architecture was developed for image-to-image translation problems.<sup>12</sup> Conditional GANs have shown great performance in translational tasks involving natural images, such as the synthesis of night views from pictures taken at daytime, generation of full object photos from edges, and maps from aerial photographs. The promise of conditional GANs has recently been translated and expanded into medical imaging, where this strategy was employed for cross modality synthesis (e.g., MRI to CT) and transformation between  $T_1$  and  $T_2$ -weighted MRI maps.<sup>14</sup>

Here, we hypothesized, that a modified conditional GAN framework could be designed and trained to learn the manifold that links between raw semisolid MT/CEST-MRF encoded images and their quantitative exchange parameter image counterparts. Moreover, we assumed that an efficient quantification could still be obtained as the number of raw MRF encoded images is reduced, thereby allowing a substantial shortening of the acquisition time. Finally, to transform the developed approach into a clinically attractive and practical protocol, we have combined the MRF acquisition block with a 3D Snapshot CEST readout module,<sup>15</sup> allowing rapid whole-brain (or any other

organ) multi-slice imaging.

## 2. Methods

### 2.1 GAN-CEST architecture

A supervised learning framework Figure 1 was designed based on the conditional GAN architecture.<sup>12</sup> The generator was a U-Net convolutional network aiming to synthesize two proton exchange parameter maps (volume fraction and exchange rate), for either the semisolid MT or the CEST compound exchangeable protons. The discriminator aimed to predict whether the images are the ‘real’ corresponding quantitative images, or a ‘fake’ (generator synthesized maps). The ground truth was obtained by a dictionary-trained fully connected semisolid MT/CEST-MRF neural-network (Figure 1b) that received the full MRF acquisition schedule as input (M=30 raw images). GAN-CEST was trained to yield the same quantitative maps by receiving only a partial subset of N=9 raw MRF encoding images as input. For the human brain imaging scenario, the water  $T_1$ ,  $T_2$ , and  $B_0$  may vary significantly in the WM/GM/tumor tissues. Thus, to improve the reliability and accuracy of the ground-truth for this case, the  $T_1$ ,  $T_2$ , and  $B_0$  maps were acquired separately, quantified, and given as an additional direct input to the reference ground truth MT/CEST-MRF network, as performed and described by Perlman et al.<sup>8</sup> Notably, these 3 maps were not given to GAN-CEST. To preserve the perceptual and quantitative content of the original quantitative images while retaining spatial continuity and smoothness in the GAN-CEST output, the following total loss ( $L_{total}$ ) function was used:

$$L_{total} = \lambda_1 L_1 + \lambda_2 L_{adv} + \lambda_3 L_{tv} + \lambda_4 L_p \quad (1)$$

Where  $L_1$  is the pixelwise  $l_1$  content loss,  $L_{adv}$  is the adversarial loss determined by the discriminator,  $L_{tv}$  is the total variation loss, and  $L_p$  is the perceptual loss.<sup>16</sup> The latter was defined as the  $l_2$  loss between the feature maps obtained from activating a

pre-trained deep convolutional network architecture (VGG19<sup>17</sup>) on the ground truth and on the GAN-CEST approximated quantitative maps.  $\lambda_{1,2,3,4}$  are the loss weights, determined using a separate validation image set (Table 1). The training was performed for 400 epochs with a batch size of 4. The learning rates of the generator and discriminator were 0.0001 and 0.0005, respectively. The method was realized in Keras<sup>18</sup> and implemented on a desktop computer equipped with a single Nvidia GeForce RTX 3080 GPU.

## 2.2 CEST phantoms

A set of L-arginine (L-arg, chemical shift = 3 ppm) phantoms was prepared by dissolving L-arg (Sigma-Aldrich, St. Louis, MO) in a pH 4 Buffer, at a concentration of 25, 50, or 100 mM. The phantoms were titrated to different pH levels between 4.0-6.0, and placed in a dedicated holder, inside a container filled with saline/PBS. The phantoms were 3D scanned twenty times at two different imaging sites (Tubingen and Boston) using two scanner models (Prisma and Skyra, Siemens Healthineers, respectively). At each scan, a different subset of 6-7 vials was used from the general range of 4-6 pH with an L-arg concentration of 25, 50, or 100 mM. The imaging was repeated after physically and randomly rotating/moving the phantom. The phantoms were independently prepared at each site.

## 2.3 Human imaging subjects

All in vivo measurements were performed under approval by the local ethics/IRB committee. Each subject gave written, informed consent before the study. A total of 17 subjects were imaged and allocated into the training, validation, or test set, as described in Table 1. The subjects were scanned at 3 imaging sites (Tubingen, Boston, and Erlangen) and were either healthy volunteers, glioblastoma (GBM) patients, or cardiac patients. The separate validation set was used for setting the hyperparameters (e.g., the number of epochs, as determined by early stopping), and the same determined training

parameters were used for all imaging scenarios (phantom, brain, and leg). The test set was designed to impose a challenging evaluation environment, aiming to explore the GAN-CEST robustness and ability to extrapolate beyond the environment of the training samples. In particular, while all training subjects were healthy volunteers, the test set included a GBM patient, a cardiac patient, and a healthy volunteer imaged at a different site and scanner model, which were not used in the training set.

## 2.4 Magnetic resonance imaging acquisition

The MRI experiments were conducted at three imaging sites using four 3T clinical scanners consisting of three different models (2×Prisma, Trio, and Skyra scanners, Siemens Healthineers) and three coil types (64-channel head coil, 32 channel head coil, and a single-element leg coil). All acquisition schedules were implemented using the Pulseseq prototyping framework<sup>19</sup> and the open-source Pulseseq-CEST sequence standard.<sup>20</sup> The MRF protocol generated  $M=30$  raw, molecular information encoding images, using a spin lock saturation train ( $13 \times 100$  ms, 50% duty-cycle), which varied the saturation pulse power between 0-4  $\mu$ T.<sup>8</sup> The saturation pulse frequency offset was fixed at 3 ppm for L-arginine phantom imaging<sup>4,21</sup> or varied between 6-14 ppm for semisolid MT brain/leg imaging.<sup>8</sup> The saturation block was fused with the 3D centric reordered EPI readout module described by Mueller et al.<sup>15</sup> and Akbey et al.,<sup>22</sup> providing a 1.8/1.8/2.5 mm isotropic resolution for phantom/whole-brain/calf-muscle imaging, respectively. The FOV was set to  $256 \times 224 \times 156$  mm<sup>3</sup>, echo time (TE)=11ms, flip angle (FA)=15°. The full 3D MRF acquisition ( $M=30$ ) took between 2:21 to 2:53 (minutes:seconds), depending on the scanner and coil configuration. For brain imaging, the same rapid readout module and hybrid pulseseq-CEST framework were used for acquiring additional  $B_0$ ,  $T_1$  and  $T_2$  maps, via WASABI,<sup>23</sup> saturation recovery, and multi-echo sequences, respectively, resulting in a total scan time of 8.5 minutes.

## 2.5 Data analysis

### 2.5.1 Phantom data preprocessing

In vitro images with no L-arginine vials, partial vials, or severe image artifacts were removed. The 239 remaining images were split into groups of 222 training images, from 20 phantom scans, and 17 test images from a different phantom. Canny edge detection and circle Hough Transforms (CHT) were used for background masking and vial segmentation, respectively, implemented in Python. Seven-fold data augmentation was performed using translations and horizontal/vertical image flips.

### 2.5.2 In vivo preprocessing

All images were motion-corrected and registered using elastix.<sup>24</sup> Gray-matter and white-matter segmentation was performed using statistical parameter mapping (SPM)<sup>25</sup> from a  $T_1$  map. Quantitative reference CEST-MRF maps were obtained using a fully connected neural network trained on simulated dictionaries, where all  $M=30$  raw input measurements were taken as input. For brain imaging, pixelwise  $T_1$ ,  $T_2$ , and  $B_0$  values were also incorporated as direct inputs to the NN. For a detailed description of the CEST-MRF reconstruction and quantification procedure see the recent publication by Perlman et al.<sup>8</sup>

### 2.5.3 Statistical analysis

Pearson's correlation coefficients were calculated using the open-source SciPy scientific computing library for Python.<sup>26</sup> The structural similarity index (SSIM)<sup>27</sup> was computed using the SSIM-python imaging library (PIL). In all box plots, the central horizontal lines represent median values, box limits represent upper (third) and lower (first) quartiles, whiskers represent  $1.5 \times$  the interquartile range above and below the upper and lower quartiles, and circles represent outliers. Statistics in the text are presented as mean  $\pm$  standard deviation. Differences were considered significant



at  $p < 0.05$ .

### 3. Results

#### 3.1 Phantom study - exchange parameter quantification performance

Representative GAN-CEST generated exchange parameter maps are shown in Figure 2a,b. An excellent agreement between the GAN-CEST generated and CEST-MRF-based L-arg concentration maps was observed, with an average normalized root mean-squared error (NRMSE) of  $1.8 \pm 0.1\%$ , a SSIM of  $0.975 \pm 0.005$  (Figure 3c,d), and a significant correlation across all slices (Pearson's  $r = 0.967$ ,  $p < 0.0001$ ) (Figure 3a). GAN-CEST generated, and CEST-MRF proton exchange rate maps were similarly correlated (Pearson's  $r = 0.961$ ,  $p < 0.0001$ , Figure 3b), with a NRMSE of  $1.9 \pm 0.1\%$  and SSIM of  $0.973 \pm 0.005$  (Figure 3c,d).

#### 3.2 Phantom study - direct estimation of concentration and pH

To explore the GAN-CEST ability for direct estimation of the pH and compound concentration, we created another set of ground-truth reference images, where all pixels in each segmented vial were replaced by the pH-meter measured pH, and the analytic-scale determined L-arg concentration. GAN-CEST was retrained while employing these images as the target, followed by an estimation of the pH and L-arg concentration in a different phantom test set (Figure 2e-h). GAN-CEST generated concentration maps were in good agreement with measured values, yielding an NRMSE of  $1.3 \pm 0.7\%$  and SSIM of  $0.976 \pm 0.005$  (Figure 3g,h) and a significant correlation across all slices (Pearson's  $r = 0.979$ ,  $p < 0.0001$ , Figure 3e). Similarly, GAN-CEST generated pH maps were in good agreement with measured values, yielding an NRMSE of  $0.6 \pm 0.4\%$  and SSIM of  $0.984 \pm 0.006$  (Figure 3g,h) and a significant correlation across all slices (Pearson's  $r = 0.997$ ,  $p < 0.0001$ ) (Figure 3f).

### 3.3 In-vivo study - brain parameter quantification

A comparison between the GAN-CEST results with the number of raw molecular encoding images set to  $N=9$  and the full-length MRF-based reference ( $M=30$ ) for four representative slices is shown in Figure 4 (healthy volunteer scanned at a site and scanner model that were not available in the training cohort) and Figure 5 (tumor patient). The accelerated GAN-CEST output was visually very similar to the CEST-MRF reference (average SSIM  $> 0.925$ , average NRMSE  $< 5.2\%$ , Figure 6c,d,g,h). Moreover, in regions with large susceptibility artifacts, GAN-CEST demonstrated improved performance and reduced noise compared to MRF (red arrows in Figures 4,5). Although the training cohort included only healthy volunteers, GAN-CEST was able to output CEST-MRF comparable parameter maps, even in complex tumor and edema containing image slices (Figure 5). The resulting WM/GM  $f_{ss}$  estimated by the GAN-CEST approach for all non-tumor-containing slices was  $18.7 \pm 2.1 / 13.2 \pm 2.5\%$ , compared to  $18.7 \pm 2.0 / 12.4 \pm 2.7\%$  using the full-length MRF. The WM/GM  $k_{ssw}$  estimated by the GAN-CEST approach was  $36.2 \pm 6.1 / 51.6 \pm 8.5$  Hz, compared to  $33.9 \pm 5.2 / 49.1 \pm 8.5$  Hz, by the full-length MRF reference, with significant correlation between individual pixel values obtained by both methods (Pearson's  $r=0.90$  and  $0.75$  for  $f_{ss}$  and  $k_{ssw}$ , respectively,  $p<0.001$ , Figure 6a,b).

### 3.4 In-vivo study - calf-muscle parameter quantification

The GAN-CEST based in-vivo calf exchange parameter quantification (Figure 7) was characterized by an SSIM  $> 0.94$  and an average NRMSE  $< 7\%$  (Figure 8). A significant correlation was observed between the GAN-predicted and reference CEST-MRF-based parameters, although the semi-solid volume fraction proton quantification was in better agreement with CEST-MRF than the exchange rate ( $r = 0.73$ ,  $p<0.001$ , and  $r=0.51$   $p<0.001$ , respectively).

### 3.5 Acquisition, training, and inference times

GAN-CEST was able to accelerate the scan time by 70% as it required the acquisition of only  $N=9$  raw molecular information encoding images instead of  $M=30$ . This translated into a CEST/MT protocol acquisition time of only 42-52 seconds, depending on the scanner model hardware and the number of coil channels. Moreover, for the brain imaging scenario, GAN-CEST circumvented the need to acquire separate  $T_1$ ,  $T_2$ , and  $B_0$  maps, providing a total acceleration of about 91% (44 seconds instead of 8.5 minutes). The total training time was 4.66 hours / 8.71 hours / 12.81 hours, and the 3D inference time was 0.29 seconds / 0.54 seconds / 0.80 seconds, for the phantom, in-vivo calf muscle, and in-vivo brain, respectively.

## 4. Discussion

In recent years, the CEST contrast mechanism has been increasingly studied for a variety of medical applications.<sup>28</sup> The molecular information provided by CEST, most commonly by the amide proton transfer (APT) effect, has provided added clinical value compared to traditional  $T_1/T_2$ -weighted imaging. For example, endogenous CEST signals have been correlated with tumor lesion enhancement following Gadolinium injection.<sup>3,29</sup> Furthermore, CEST-weighted images were able to better discriminate treatment related changes from tumor progression.<sup>30</sup> MT signals stemming from semisolid macromolecules have also been shown to be beneficial for cancer characterization and monitoring, either as a standalone method<sup>31</sup> or in combination with CEST.<sup>32</sup> In addition, MT has demonstrated potential as a biomarker for pathological skeletal muscle<sup>33</sup> and has long been known for its importance for multiple sclerosis (MS) imaging.<sup>34</sup> However, both CEST and semisolid MT imaging are highly sensitive to the acquisition parameters used, as well as to changes in water pool relaxation. Moreover, these methods are prone to bias stemming from the analysis metric used and are subjected to contaminations from the signals originating from other tissue metabolites and com-

pounds.<sup>35</sup> All the aforementioned challenges have motivated the development of quantitative approaches for semisolid MT/CEST imaging.<sup>36,37</sup> In the context of clinical imaging, it is clearly important to also strive for short acquisition times. Semisolid MT/CEST MRF has recently been suggested as a rapid and quantitative molecular imaging pipeline.<sup>10</sup> However, as the multi-protocol conventional clinical routine is already lengthy (e.g., 30-40 minutes for each GBM patient monitoring session), it is essential to further accelerate semisolid MT/CEST MRF, rendering it a cost-effective addition to clinical imaging protocols. The methodology proposed in this paper has made several contributions towards that cause. (1) The CEST-MRF saturation block was fused with a highly efficient and rapid snap-shot readout, allowing 3D semisolid-MT or CEST-MRF acquisition in about 3 minutes, or 8.5 minutes (when  $B_0$ ,  $T_1$ , and  $T_2$  maps are also acquired based on the same 3D readout). (2) It employed generative adversarial networks to further accelerate the 3D molecular scan time by reducing the required number of signal trajectory acquisitions by 70%, requiring acquisition times of less than 1 min. (3) The GAN-CEST images have demonstrated the ability to mitigate the noise arising from field inhomogeneity and susceptibility artifacts (e.g., near the sinuses and the eyes, Figure 4,5). (4) The GAN-CEST was able to extrapolate beyond the training data properties, as demonstrated using a subject scanned at a site and scanner model that were not used for training (Figure 4, Figure 6e-h).

In terms of the reconstruction (or parameter quantification from raw MRF images), one of the main limitations of "classical fingerprinting", is the lengthy dictionary matching times, where millions of simulated signals need to be compared to the experimental images (e.g., by means of a pixelwise dot-product matching). The framework presented here allows the reconstruction of quantitative proton volume fraction and exchange rate maps of the entire 3D volume acquired, in less than a second. Pixelwise matching using fully connected neural networks has previously been used for rapid semisolid MT/CEST MRF reconstruction.<sup>8</sup> However, the use of the GAN architecture, with its inherent spatial dependencies and U-Net structure, has also provided the ability

to mitigate susceptibility artifacts (Figure 4,5).

The semi-solid proton exchange rate was generally slower in the GAN-CEST-based images, compared to CEST-MRF, in the tumor regions (Figure 5i-p), as well as in some anatomical parts of the calf (Figure 7i-k). This is in line with previous quantification attempts that faced similar challenges and reduced accuracy with the semisolid MT exchange rate.<sup>9,38</sup> These reports have attributed the poor discrimination ability for this property to the relatively small signal fluctuations that were observed as the exchange rate was varied. In this work, the reduced accuracy can also be explained by the intentionally challenging data sets design, where tumor data were not provided during the training. This assumption is supported by the increased correlation observed between the CEST-MRF and GAN-CEST exchange rates for a healthy volunteer that was evaluated (Figure 4, and Figure 6f compared to Figure 6b). The phantom data quantitative exchange parameter maps obtained using GAN-CEST with 70% acceleration were in excellent agreement with the CEST-MRF-based reference (Figures 2,3). Moreover, the same GAN architecture has allowed the direct estimation of the pH and compound concentration, measured using gold-standard non-MRI measures (pH-meter and analytical scale). The worst performance was obtained for the vial containing pH=4 (Figure 3e,f). This is not surprising, given the base-catalyzed exchange rate of L-arginine, which results in small CEST signal amplitudes at low pH due to the slow exchange rate. While direct mapping from raw CEST data to pH is very attractive, future work should explore methods for obtaining in-vivo ground-truth reference pH data.

There is a tradeoff between the level of acceleration (manifested by the number of raw MRF images acquired,  $N$ ) and the parameter quantification performance. For example, increasing  $N$  from 9 to 20, improves the GAN-CEST visual similarity between the tumor semisolid MT proton exchange rate, and those obtained by CEST-MRF (Supplementary Information Figure S1). Similarly, the  $k_{ssw}$  NRMSE decreased from  $0.052 \pm 0.014$  using 9 input images to  $0.045 \pm 0.013$ , using 20 input images. In addition, the correlation between the non-tumor tissue exchange parameters for GAN-

CEST compared to CEST-MRF is improved from  $r=0.90$  ( $p<0.001$ ) and  $0.75$  ( $p<0.001$ ) for 9 input images, to  $r=0.92$  ( $p<0.001$ ) and  $0.77$  ( $p<0.001$ ) using 20 input images. While the quantitative maps obtained with a drastic acceleration of 70% are deemed both visually and quantitatively satisfactory, future expanded clinical evaluations could determine more accurately the degree of acceleration level sufficient for retaining a correct diagnosis.

Several additional steps could improve the GAN-CEST performance. First, the training set used here was intentionally composed of healthy volunteers only, aimed to examine the extrapolation ability of the method. In addition, although 3D acquisitions create a large number of images, the number of training subjects scanned was relatively small (Table 1). Significantly increasing the training cohort, and training on a variety of pathological cases, are expected to boost the accuracy of the method. Second, the proposed method performance is dependent on the original discrimination ability of the M-length acquisition schedule. The parameter discrimination ability could be further improved, while benefiting from the spatial denoising and extrapolation capabilities demonstrated here, by combining the proposed GAN-CEST approach with an optimized acquisition schedule.<sup>39,40</sup>

## 5. Conclusion

The GAN-CEST framework has demonstrated the ability to accelerate 3D acquisitions of semisolid MT and CEST mapping by 70% while maintaining excellent agreement with full-length CEST-MRF based reference maps and retaining performance across unseen pathologies and scanner models. Furthermore, GAN-CEST has shown improvements over CEST-MRF in regions with large susceptibility artifacts. GAN-CEST has exhibited promising initial results in direct estimation of compound concentration and pH from MRF encoded images.

## **Acknowledgment**

The work was supported by the US National Institutes of Health Grants R01-CA203873, R01-EB03008, and P41-RR14075. The research was supported by a CERN openlab cloud computing grant. This project has received funding from the European Union's Horizon 2020 research and innovation programme under the Marie Skłodowska-Curie grant agreement No 836752 (OncoViroMRI). This paper reflects only the author's view, and the European Research Executive Agency is not responsible for any use that may be made of the information it contains.

## **Data availability statement**

The MRI acquisition schedule pre-saturation blocks used in this paper are available in the Pulseseq-CEST open-source format<sup>20</sup> at <https://github.com/kherz/pulseseq-cest-library>, under the folders MRF\_CEST\_Larginine\_3T\_002\_13SL\_DC50\_2500ms and MRF\_CEST\_MT\_3T\_003\_13SL\_DC50\_2500ms. All fully trained networks required to reproduce the GAN-based CEST/MT reconstruction presented in this work are available at <https://doi.org/10.6084/m9.figshare.20346369>, as well as a sample phantom dataset. The full 3D human data used in this work are not publicly available due to participant/patient privacy. For additional inquiries please contact the corresponding author.

## References

- [1] Henkelman RM, Stanisz GJ, Graham SJ. Magnetization transfer in MRI: a review *NMR in Biomedicine*. 2001;14:57–64.
- [2] Zijl Peter CM, Lam Wilfred W, Xu Jiadi, Knutsson Linda, Stanisz Greg J. Magnetization transfer contrast and chemical exchange saturation transfer MRI. Features and analysis of the field-dependent saturation spectrum *Neuroimage*. 2018;168:222–241.
- [3] Jones Kyle M, Pollard Alyssa C, Pagel Mark D. Clinical applications of chemical exchange saturation transfer (CEST) MRI *Journal of Magnetic Resonance Imaging*. 2018;47:11–27.
- [4] Cohen Ouri, Huang Shuning, McMahon Michael T, Rosen Matthew S, Farrar Christian T. Rapid and quantitative chemical exchange saturation transfer (CEST) imaging with magnetic resonance fingerprinting (MRF) *Magnetic Resonance in Medicine*. 2018;80:2449–2463.
- [5] Ma Dan, Gulani Vikas, Seiberlich Nicole, et al. Magnetic resonance fingerprinting *Nature*. 2013;495:187–192.
- [6] Zhou Zhengwei, Han Pei, Zhou Bill, et al. Chemical exchange saturation transfer fingerprinting for exchange rate quantification *Magnetic Resonance in Medicine*. 2018;80:1352–1363.
- [7] Heo Hye-Young, Han Zheng, Jiang Shanshan, Schar Michael, Zijl Peter CM, Zhou Jinyuan. Quantifying amide proton exchange rate and concentration in chemical exchange saturation transfer imaging of the human brain *Neuroimage*. 2019;189:202–213.
- [8] Perlman Or, Ito Hirotaka, Herz Kai, et al. Quantitative imaging of apoptosis fol-



lowing oncolytic virotherapy by magnetic resonance fingerprinting aided by deep learning *Nature Biomedical Engineering*. 2022;6:648–657.

- [9] Kang Beomgu, Kim Byungjai, Schar Michael, Park HyunWook, Heo Hye-Young. Unsupervised learning for magnetization transfer contrast MR fingerprinting: Application to CEST and nuclear Overhauser enhancement imaging *Magnetic Resonance in Medicine*. 2021;85:2040–2054.
- [10] Perlman Or, Farrar Christian T, Heo Hye-Young. MR fingerprinting for semisolid magnetization transfer and chemical exchange saturation transfer quantification *NMR in Biomedicine*. 2022:e4710.
- [11] Creswell Antonia, White Tom, Dumoulin Vincent, Arulkumaran Kai, Sengupta Biswa, Bharath Anil A. Generative adversarial networks: An overview *IEEE Signal Processing Magazine*. 2018;35:53–65.
- [12] Isola Phillip, Zhu Jun-Yan, Zhou Tinghui, Efros Alexei A. Image-to-image translation with conditional adversarial networks in *Proceedings of the IEEE Conference on Computer Vision and Pattern Recognition*:1125–1134 2017.
- [13] Goodfellow Ian, Pouget-Abadie Jean, Mirza Mehdi, et al. Generative adversarial nets *Advances in Neural Information Processing Systems*. 2014;27.
- [14] Yi Xin, Walia Ekta, Babyn Paul. Generative adversarial network in medical imaging: A review *Medical Image Analysis*. 2019;58.
- [15] Mueller Sebastian, Stirnberg Rudiger, Akbey Suzan, et al. Whole brain snapshot CEST at 3T using 3D-EPI: Aiming for speed, volume, and homogeneity *Magnetic Resonance in Medicine*. 2020;84:2469–2483.
- [16] Johnson Justin, Alahi Alexandre, Fei-Fei Li. Perceptual losses for real-time style transfer and super-resolution in *European Conference on Computer Vision*:694–711Springer 2016.

- [17] Simonyan Karen, Zisserman Andrew. Very deep convolutional networks for large-scale image recognition *arXiv preprint arXiv:1409.1556*. 2014.
- [18] Gulli Antonio, Pal Sujit. *Deep learning with Keras*. Packt Publishing Ltd 2017.
- [19] Layton Kelvin J, Kroboth Stefan, Jia Feng, et al. Pulseq: a rapid and hardware-independent pulse sequence prototyping framework *Magnetic Resonance in Medicine*. 2017;77:1544–1552.
- [20] Herz Kai, Mueller Sebastian, Perlman Or, et al. Pulseq-CEST: Towards multi-site multi-vendor compatibility and reproducibility of CEST experiments using an open-source sequence standard *Magnetic Resonance in Medicine*. 2021;86:1845–1858.
- [21] Perlman Or, Herz Kai, Zaiss Moritz, Cohen Ouri, Rosen Matthew S, Farrar Christian T. CEST MR-Fingerprinting: Practical considerations and insights for acquisition schedule design and improved reconstruction *Magnetic Resonance in Medicine*. 2020;83:462–478.
- [22] Akbey Suzan, Ehse Philipp, Stirnberg Rudiger, Zaiss Moritz, Stocker Tony. Whole-brain snapshot CEST imaging at 7 T using 3D-EPI *Magnetic Resonance in Medicine*. 2019;82:1741–1752.
- [23] Schuenke Patrick, Windschuh Johannes, Roeloffs Volkert, Ladd Mark E, Bachert Peter, Zaiss Moritz. Simultaneous mapping of water shift and B1 (WASABI)—application to field-inhomogeneity correction of CEST MRI data *Magnetic Resonance in Medicine*. 2017;77:571–580.
- [24] Klein Stefan, Staring Marius, Murphy Keelin, Viergever Max A, Pluim Josien PW. Elastix: a toolbox for intensity-based medical image registration *IEEE Transactions on Medical Imaging*. 2009;29:196–205.

- [25] Ashburner John, Friston Karl J. Unified segmentation *Neuroimage*. 2005;26:839–851.
- [26] Virtanen Pauli, Gommers Ralf, Oliphant Travis E, et al. SciPy 1.0: fundamental algorithms for scientific computing in Python *Nature Methods*. 2020;17:261–272.
- [27] Wang Zhou, Bovik Alan C, Sheikh Hamid R, Simoncelli Eero P. Image quality assessment: from error visibility to structural similarity *IEEE Transactions on Image Processing*. 2004;13:600–612.
- [28] Zhou Jinyuan, Heo Hye-Young, Knutsson Linda, Zijl Peter CM, Jiang Shanshan. APT-weighted MRI: Techniques, current neuro applications, and challenging issues *Journal of Magnetic Resonance Imaging*. 2019;50:347–364.
- [29] Zhou Jinyuan, Zhu He, Lim Michael, et al. Three-dimensional amide proton transfer MR imaging of gliomas: initial experience and comparison with gadolinium enhancement *Journal of Magnetic Resonance Imaging*. 2013;38:1119–1128.
- [30] Zhou Jinyuan, Tryggestad Erik, Wen Zhibo, et al. Differentiation between glioma and radiation necrosis using molecular magnetic resonance imaging of endogenous proteins and peptides *Nature Medicine*. 2011;17:130–134.
- [31] Mehrabian H, Lam WW, Myrehaug SD, et al. Quantitative MRI Metrics Differentiating Radioresistant from Radiosensitive Brain Metastases *International Journal of Radiation Oncology, Biology, Physics*. 2020;108:S61.
- [32] Chan Rachel W, Chen Hanbo, Myrehaug Sten, et al. Quantitative CEST and MT at 1.5 T for monitoring treatment response in glioblastoma: early and late tumor progression during chemoradiation *Journal of Neuro-Oncology*. 2021;151:267–278.

- [33] Sinclair Christopher DJ, Samson Rebecca S, Thomas David L, et al. Quantitative magnetization transfer in in vivo healthy human skeletal muscle at 3 T *Magnetic Resonance in Medicine*. 2010;64:1739–1748.
- [34] Filippi Massimo, Agosta Federica. Magnetization transfer MRI in multiple sclerosis *Journal of Neuroimaging*. 2007;17:22S–26S.
- [35] Zaiss Moritz, Windschuh Johannes, Paech Daniel, et al. Relaxation-compensated CEST-MRI of the human brain at 7 T: unbiased insight into NOE and amide signal changes in human glioblastoma *Neuroimage*. 2015;112:180–188.
- [36] Ji Yang, Zhou Iris Yuwen, Qiu Bensheng, Sun Phillip Zhe. Progress toward quantitative in vivo chemical exchange saturation transfer (CEST) MRI *Israel Journal of Chemistry*. 2017;57:809–824.
- [37] Sled John G, Pike G Bruce. Quantitative imaging of magnetization transfer exchange and relaxation properties in vivo using MRI *Magnetic Resonance in Medicine*. 2001;46:923–931.
- [38] Kim Byungjai, Schar Michael, Park HyunWook, Heo Hye-Young. A deep learning approach for magnetization transfer contrast MR fingerprinting and chemical exchange saturation transfer imaging *Neuroimage*. 2020;221:117165.
- [39] Perlman Or, Zhu Bo, Zaiss Moritz, Rosen Matthew S, Farrar Christian T. An end-to-end AI-based framework for automated discovery of rapid CEST/MT MRI acquisition protocols and molecular parameter quantification (AutoCEST) *Magnetic Resonance in Medicine*. 2022;87:2792–2810.
- [40] Kang Beomgu, Kim Byungjai, Park HyunWook, Heo Hye-Young. Learning-based optimization of acquisition schedule for magnetization transfer contrast MR fingerprinting *NMR in Biomedicine*. 2022;35:e4662.

## Tables and figures

Table 1: Human imaging data cohort

Imaging Scenario	Properties	Training Set	Validation Set	Test Set
Brain	No. subjects	5 healthy volunteers	2 GBM patients	1 GBM patient and 1 healthy volunteer
Brain	No. images*	611	166	164 (85 - patient, 79 - volunteer)
Brain	Scanner/coil/site	Prisma (64-channel, Boston) Prisma (64 channel, Tübingen) Skyra (64-channel, Boston)	Skyra (32 channel, Boston)	Prisma (64 channel, Erlangen) and Trio (32 channel, Erlangen)
Calf	No. subjects	7 healthy volunteers	—	1 cardiac patient
Calf	No. images*	416	—	52
Calf	Scanner/coil/site	Prisma/single element coil/Boston	—	Prisma/single element coil/Boston

\*7-fold data augmentation was performed using translations and horizontal/vertical image flips. The numbers mentioned in the table represent the acquired images prior to augmentation. GBM = glioblastoma.

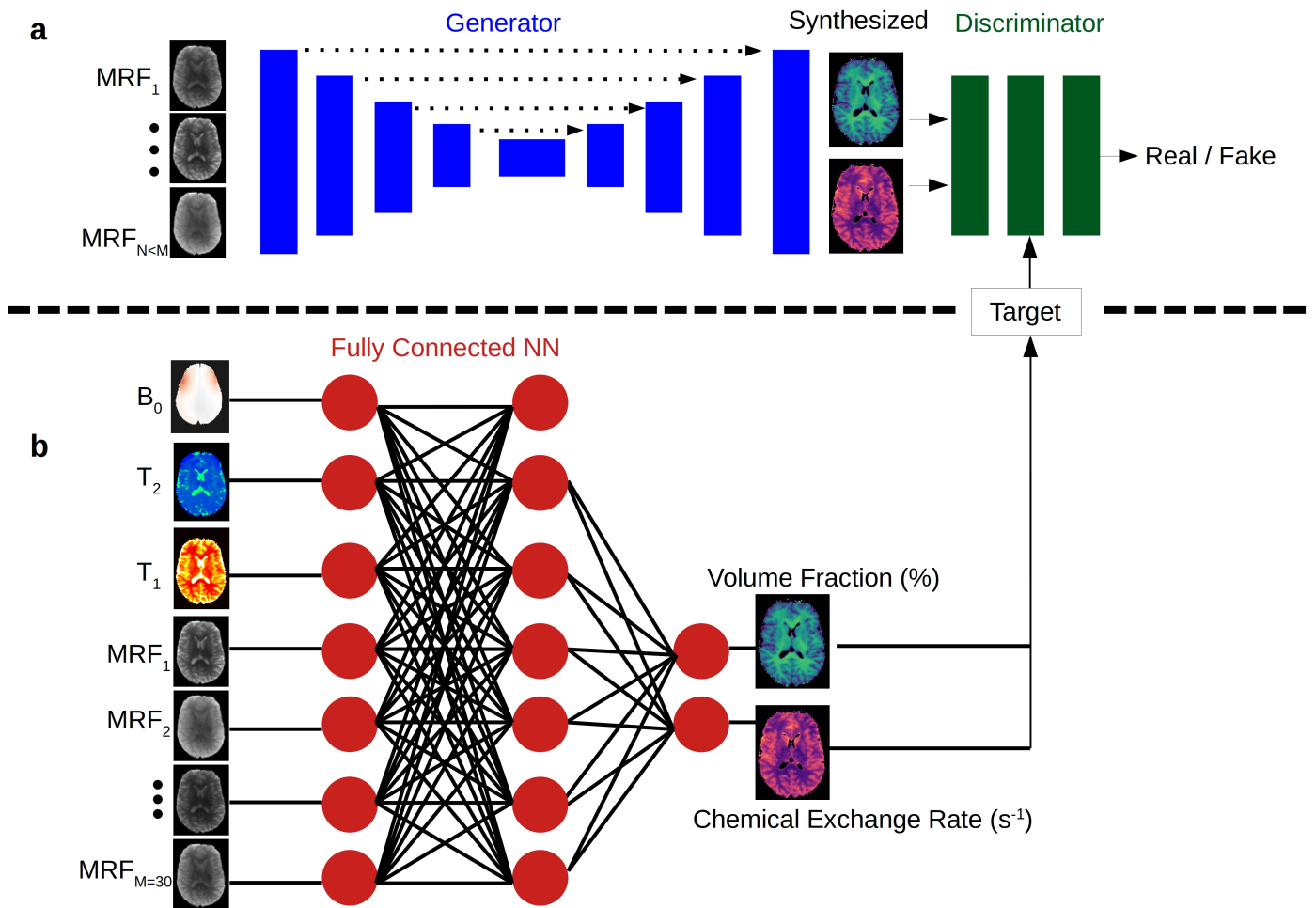


**Figure 1:** GAN-CEST architecture. a. A conditional GAN framework, receives  $N$  raw, molecular information encoding semisolid MT/CEST images, and is trained to simultaneously output the quantitative proton volume fraction and the exchange rate maps. b. A fully connected neural network, receiving the full-length raw MRF image series ( $M > N$ ) pixelwise, as well as  $T_1$ ,  $T_2$ , and  $B_0$  maps, and yielding the reference proton volume fraction and exchange rate maps.<sup>8</sup> The output of this network was used for training GAN-CEST.

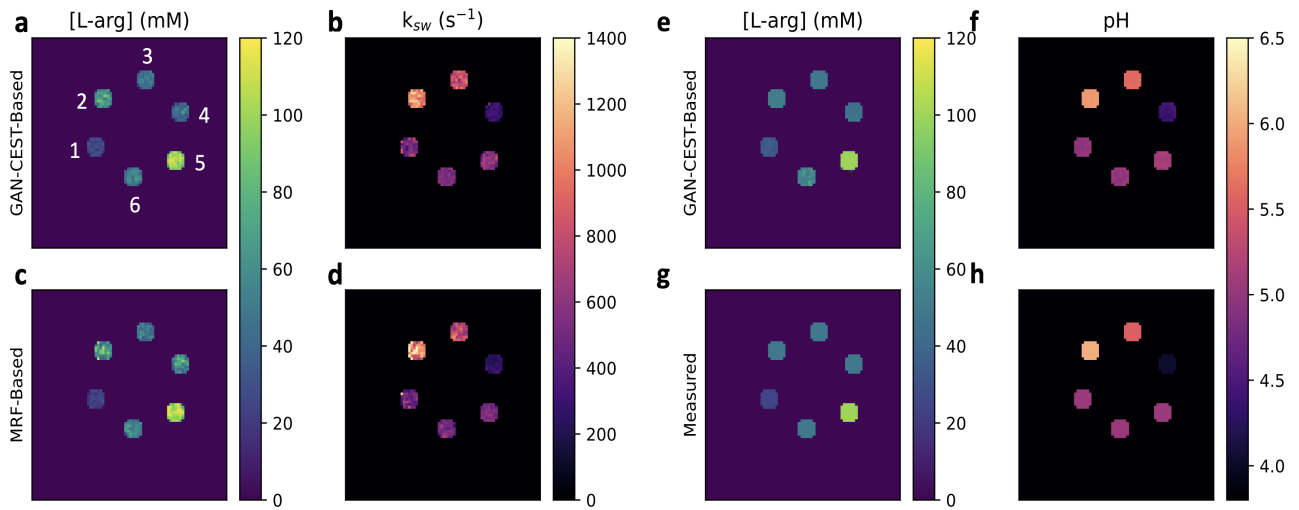


**Figure 2:** GAN-CEST in-vitro image results. a-b. L-arginine concentration (a) and exchange rate (b) maps from GAN-CEST based reconstruction, obtained with  $N=9$ . Vials are numbered 1-6. c-d. Full-length CEST-MRF based L-arginine concentration (c) and exchange rate (d) maps, obtained with  $M=30$ . e-f. GAN-CEST based ( $N=9$ ) concentration (e) and pH (f) maps. g-h. Concentration (g) and pH (h) maps, obtained using gold-standard non-MRI measures.

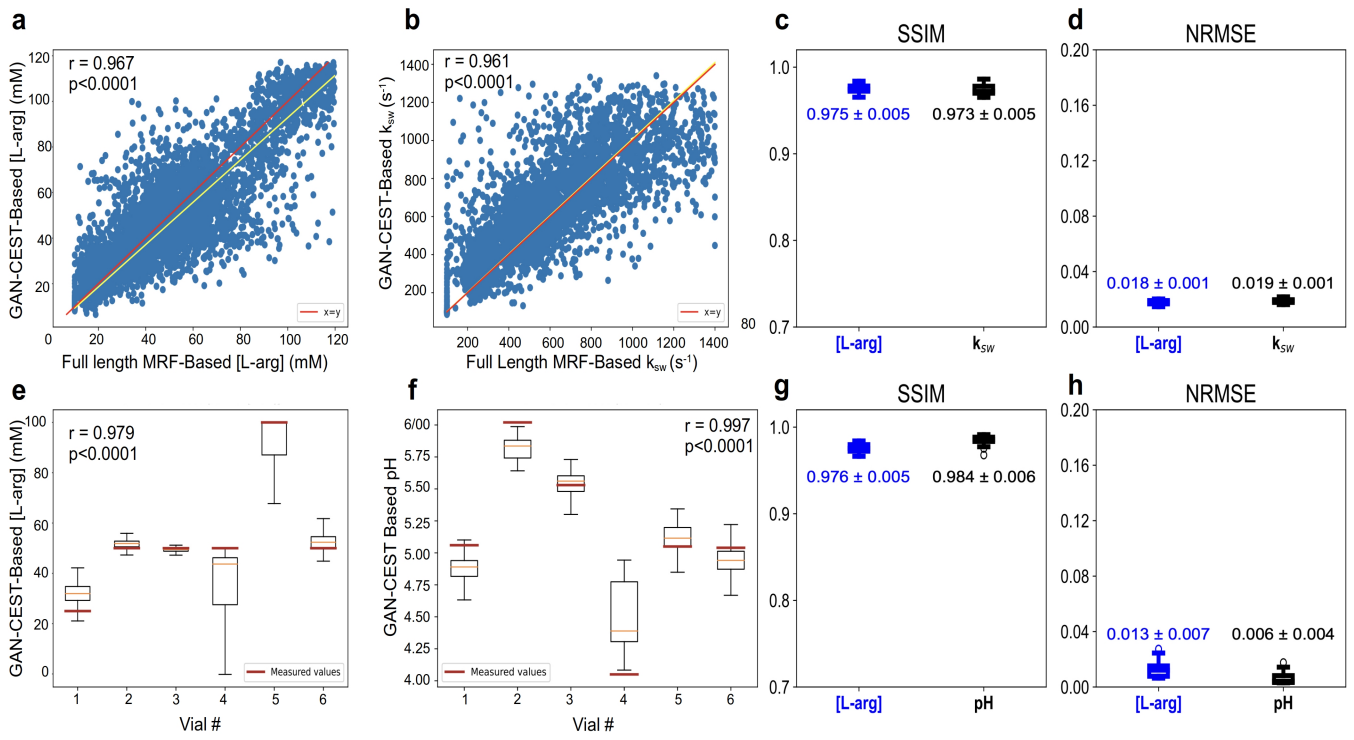


**Figure 3:** Statistical analysis and quantitative assessment of GAN-CEST performance in-vitro. a-b. Correlation between GAN-CEST based and CEST-MRF based concentration (a) and exchange rate (b) maps across the entire 3D volume of an L-arginine phantom. e-f. Box plots showing the distribution of per-vial GAN-CEST based L-arg concentration (e) and pH (f) maps with measured values indicated. Vial numbers are based on Figure 2a. c,d,g,h. Structural similarity index (SSIM) and normalized root mean squared error (NRMSE) for concentration/exchange rate (c,d) and concentration/pH (g,h) maps.



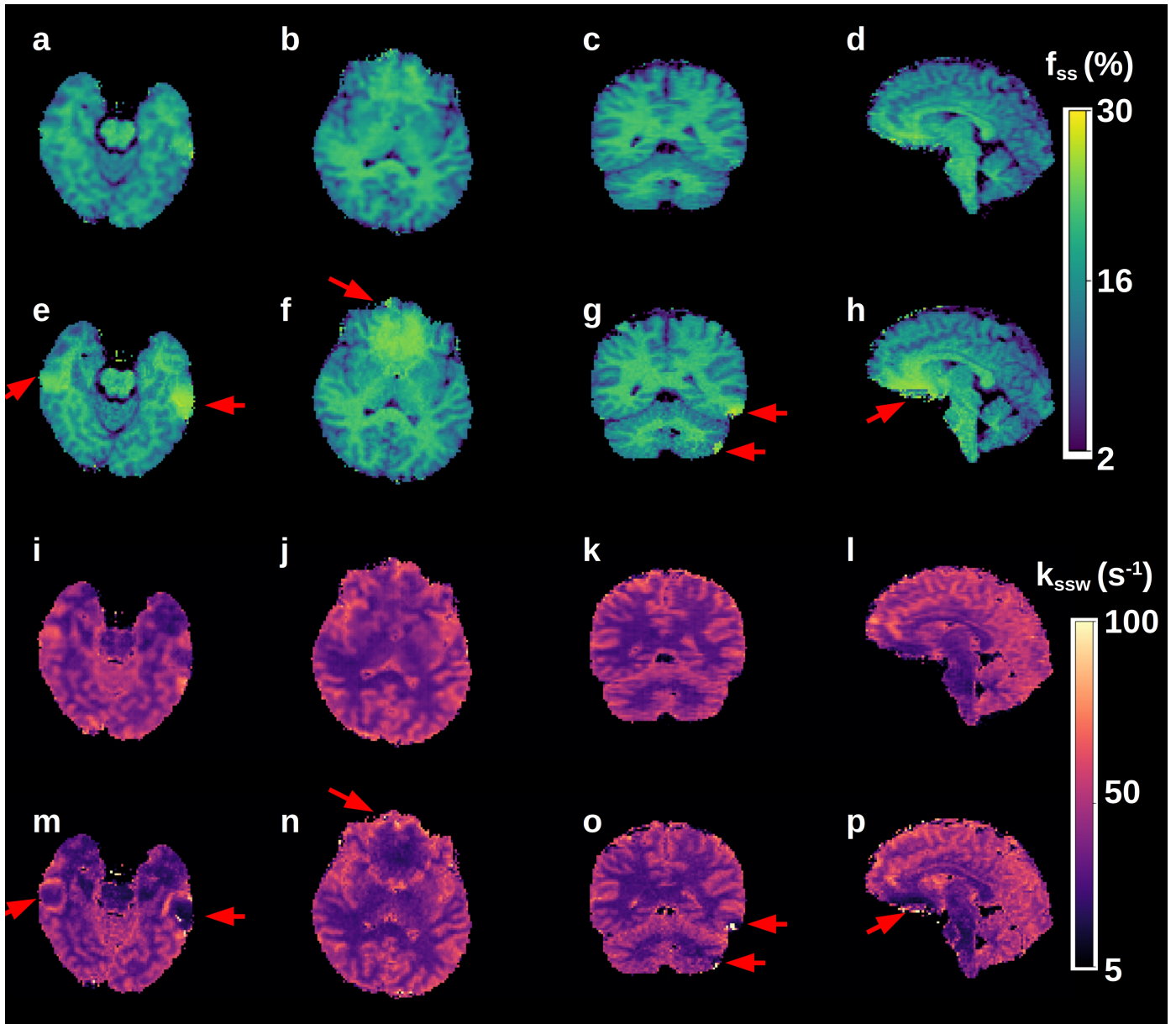


**Figure 4:** Quantitative semisolid MT parameter maps from a healthy volunteer, scanned at a site and scanner model that were not used during training. a-d. GAN-CEST based semisolid MT proton volume fraction maps, obtained with  $N=9$ . e-h. CEST-MRF-based semisolid MT proton volume fraction maps, obtained with  $M=30$ . i-l. GAN-CEST based semisolid MT proton exchange rate maps, obtained with  $N=9$ . e-h. CEST-MRF-based semisolid MT proton exchange rate maps, obtained with  $M=30$ . The red arrows indicate regions with susceptibility artifacts.

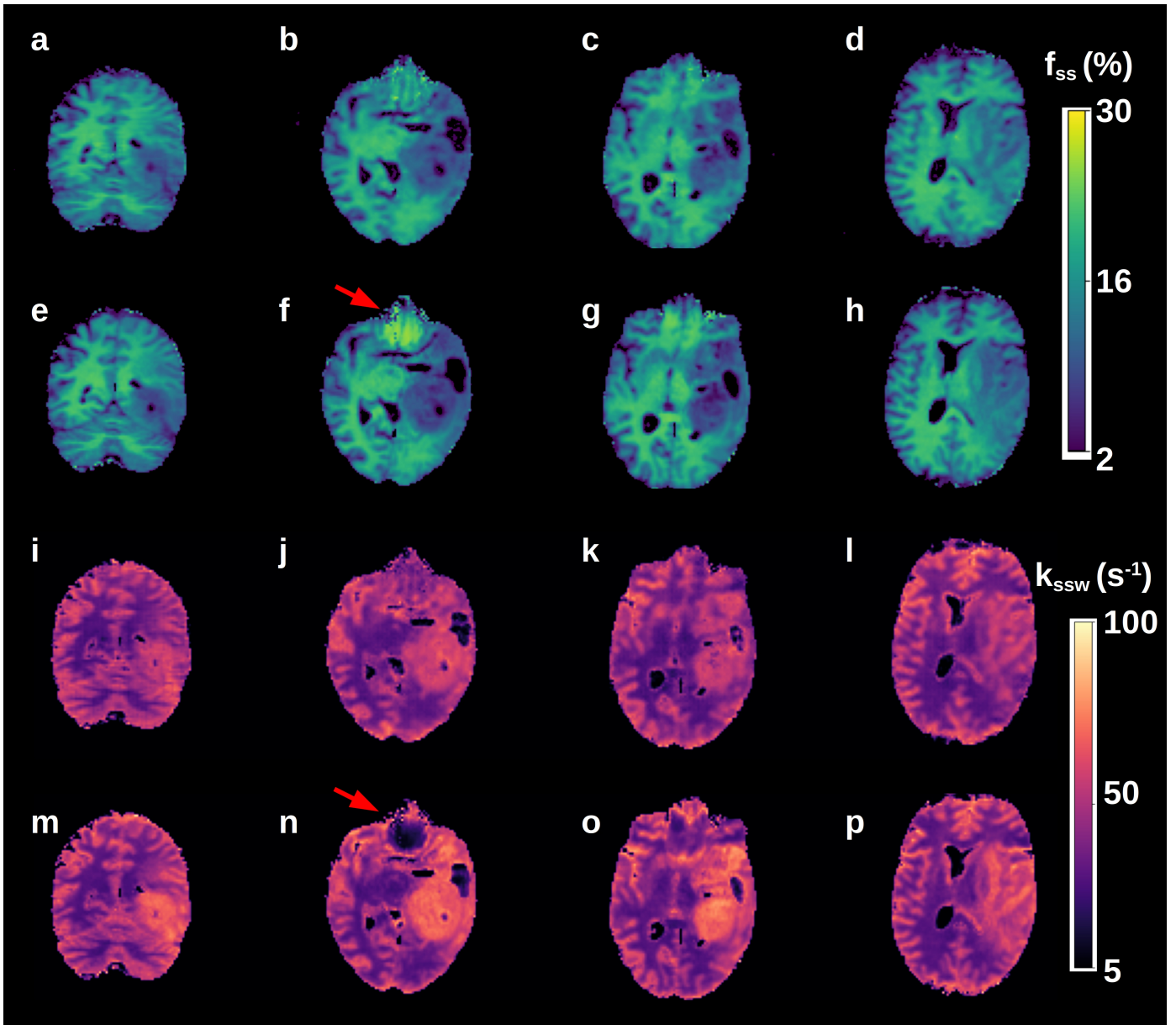


**Figure 5:** Quantitative semisolid MT parameter maps from a GBM patient. a-d. GAN-CEST based semisolid MT proton volume fraction maps, obtained with  $N=9$ . e-h. CEST-MRF-based semisolid MT proton volume fraction maps, obtained with  $M=30$ . i-l. GAN-CEST based semisolid MT proton exchange rate maps, obtained with  $N=9$ . e-h. CEST-MRF-based semisolid MT proton exchange rate maps, obtained with  $M=30$ . The red arrows indicate regions with susceptibility artifacts.

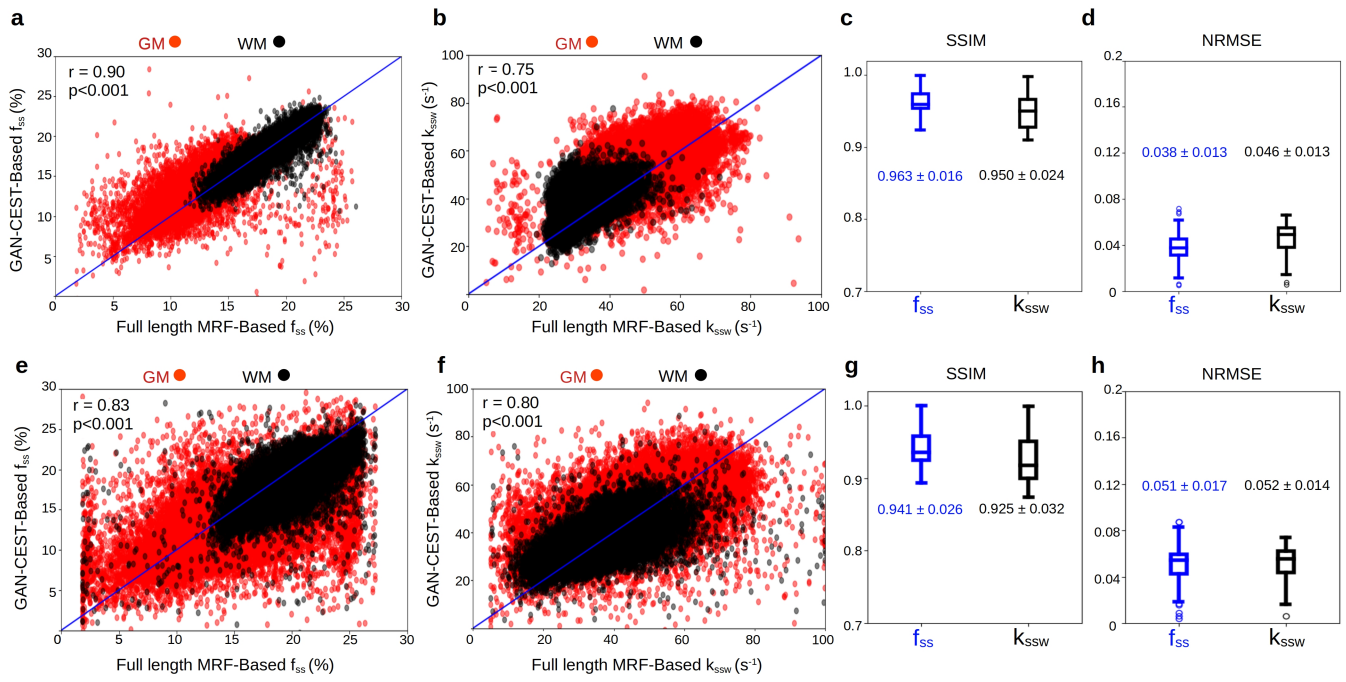


**Figure 6:** Statistical analysis and quantitative assessment of the GAN-CEST performance in the in-vivo brains of a tumor patient (a-d) and a healthy volunteer (e-h). a-b. Correlation between all GAN-CEST based proton semisolid MT proton volume fractions (a) and exchange rates (b) for the entire brain in the WM/GM, and the corresponding pixel values obtained using CEST-MRF. e,f. A similar analysis for the healthy human volunteer scanned at a site and scanner that were not available during training. c,d,g,h. Structural similarity index metric (SSIM) and normalized root mean squared error (NRMSE) for the tumor patient (c-d) and healthy volunteer (g-h).

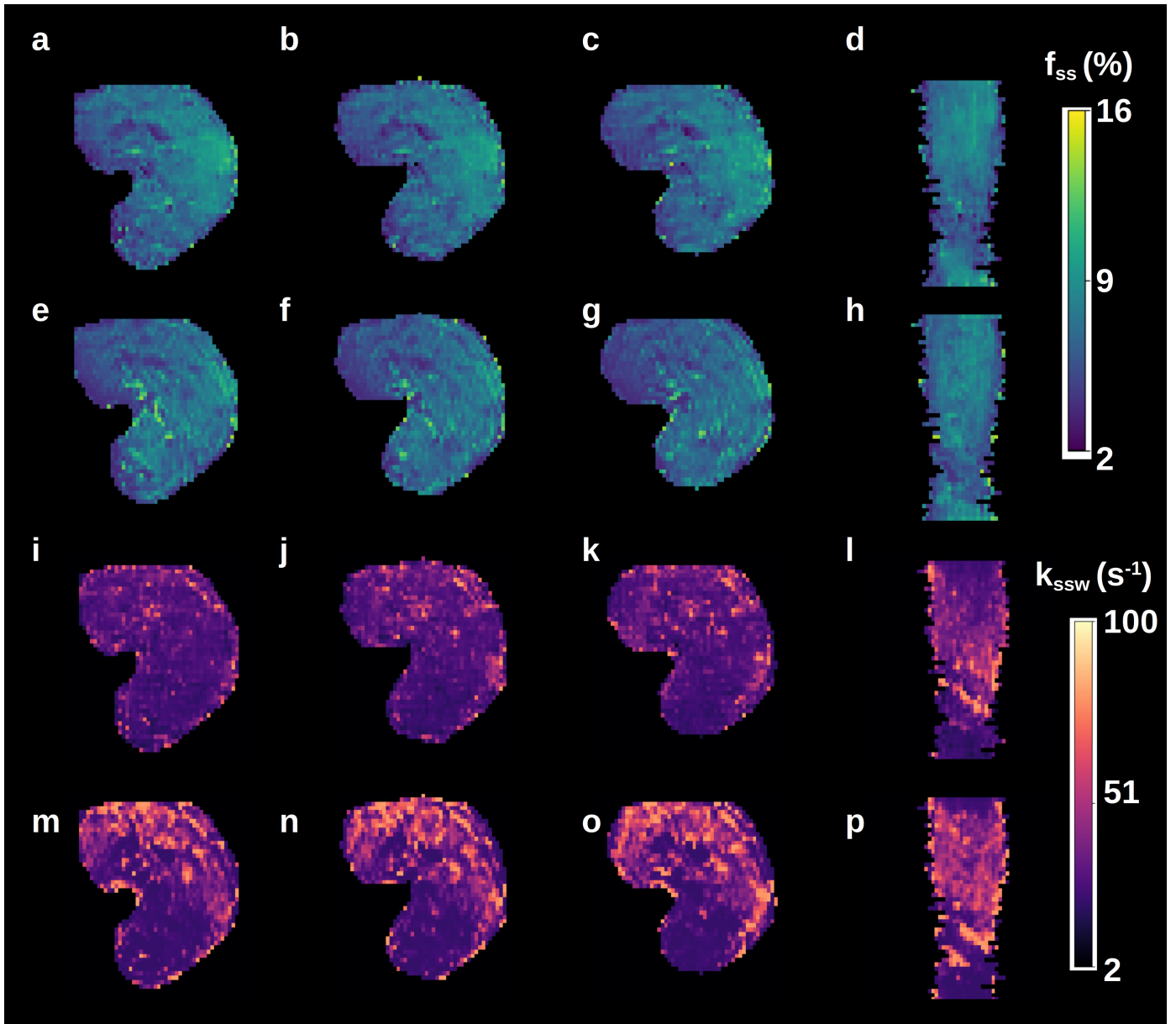


**Figure 7:** Quantitative semisolid MT parameter maps from the calf muscle of a cardiac patient. a-d. GAN-CEST based semisolid MT proton volume fraction maps, obtained with  $N=9$ . e-h. CEST-MRF-based semisolid MT proton volume fraction maps, obtained with  $M=30$ . i-l. GAN-CEST based semisolid MT proton exchange rate maps, obtained with  $N=9$ . m-p. CEST-MRF-based semisolid MT proton exchange rate maps, obtained with  $M=30$ .

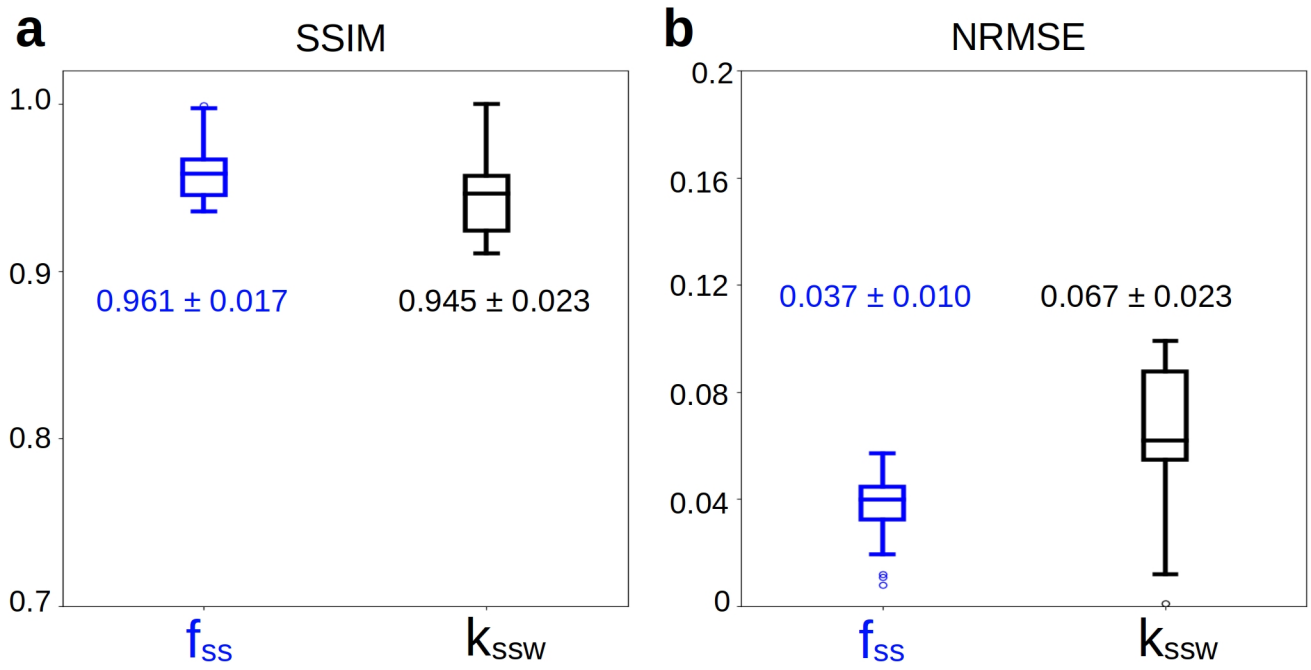


**Figure 8:** Statistical analysis and quantitative assessment of the GAN-CEST performance in the calf-muscle of a cardiac patient. a. Structural similarity index metric (SSIM). b. Normalized root mean squared error (NRMSE).